J. Fluid Mech. (2012), *vol.* 711, *pp.* 40–60.
doi:10.1017/jfm.2012.362

Transition scenario of a sphere freely falling in a vertical tube

Thibaut Deloze†, Yannick Hoarau and Jan Dušek

Institut de Mécanique des Fluides et des Solides, Université de Strasbourg/CNRS, 67000 Strasbourg, France

(Received 12 December 2011; revised 10 May 2012; accepted 15 July 2012; first published online 20 September 2012)

The paper presents the results of direct numerical simulations of the fall of a single freely moving sphere in a vertical circular tube. Most results are obtained for the solid–fluid density ratio $\rho_s/\rho = 2$. The parametric investigation is carried out depending on the Galileo number defined in Jenny, Dušek & Bouchet *J. Fluid Mech.*, vol. 508, 2004, pp. 201–239. A qualitatively new scenario is found, as compared to that of an unconfined sphere. The primary bifurcation making the sphere deviate from a vertical fall along the tube axis at a constant velocity is of Hopf type. It sets in at a Galileo number (between 155 and 160) similar to that for an unconfined sphere. We find evidence for two stages of the primary regime: a planar trajectory at $G = 160$ and a helical one (at $G = 165$ and 170). At these Galileo numbers, the regime is perfectly periodic, with a slow period corresponding to a Strouhal number only slightly above 0.01. The dynamics is identified as a periodic wake–wall interaction. The helical regime is found to give way directly to chaos between $G = 170$ and $G = 180$. This transition is associated with the onset of vortex shedding in the wake of the falling sphere and with a complex interaction between the unsteady wake and the wall marked by intermittent wake extinction. The effect of density ratio is partly investigated at $G = 250$ by considering three density ratios: 2, 3 and 5. A significant change of behaviour is found between the ratios 3 and 5.

Key words: nonlinear dynamical systems, particle/fluid flows, transition to turbulence

1. Introduction

In recent years, a large amount of numerical and experimental work has provided good insight into the scenario of transition of an unconfined freely moving sphere under the combined action of gravity, buoyancy and hydrodynamic force. It has been shown (see Jenny, Bouchet & Dušek 2003) that the degrees of freedom of the free body only slightly modify the actual onset of the transition but, for ascending spheres, yield a scenario significantly different (see Jenny & Dušek 2004; Veldhuis & Biesheuvel 2007) from that found in a fixed sphere wake as reported by Johnson & Patel (1999), Ormières & Provansal (1999), Ghidersa & Dušek (2000) and Tomboulides & Orszag (2000). Much less is known about a sphere experiencing interaction with walls. Such a configuration is, however, prototypical of a two-phase transport problem, and has therefore received at least as much attention as that of an unconfined sphere.

† Email address for correspondence: deloze@unistra.fr

Segré (1961) and Segré & Silberberg (1962) investigated experimentally a suspension of small neutrally buoyant spheres in a Poiseuille pipe flow and reported an equilibrium radial position at 0.6 radii from the pipe axis. Later work (e.g. Karnis, Goldsmith & Mason 1966) focused on non-neutrally buoyant spheres and the effect of slip velocity on the equilibrium radius. More recently, experimental work by Matas, Morris & Guazzelli (2004) confirmed the results obtained for neutrally buoyant spheres at low Reynolds numbers (based on the pipe diameter) and showed that at higher Reynolds numbers the equilibrium annulus moves toward the wall. Moreover, Matas *et al.* report the existence of a second equilibrium position closer to the pipe axis. For all its practical importance, this configuration is rather difficult to explore numerically and theoretically. Results of a simulation of a neutrally buoyant sphere at a very low Reynolds number ($Re = 0.4$) for the pipe flow have been published by Yang *et al.* (2005). They yield an equilibrium position at 0.5 radii. The cited work, however, provides more a proof of feasibility of the simulation than a deeper physical analysis, which might be explained by the numerical costs. Some investigations have therefore been attempted in two-dimensional configurations (e.g. Feng, Hu & Joseph 1994; Yu *et al.* 2002). They show a strong dependence of the equilibrium position on the (cylindrical) particle density and predict an equilibrium position in the symmetry plane of the channel for all sedimenting particles. This does not seem to contradict experimental and numerical three-dimensional results because it is well known that sedimenting cylinders behave differently to sedimenting spheres (see Namkoong, Yoo & Choi 2008).

Because of the complexity of the configuration, attempts have been made to shed light on the Segré–Silberberg effect by analysing its partial mechanisms. The shear might provide a likely explanation if it can be shown that for some shear the lift becomes zero. For non-buoyant spheres, the problem can be reformulated as that of lift of a sphere moving at constant velocity in a shear flow. The sphere velocity can be characterized by the Reynolds number $Re = Ud/\nu$, where U is the flow velocity at the sphere's centre, d is the sphere diameter, and ν is the kinematic viscosity of the fluid. The shear is given by the shear rate $s = (\mathrm{d}U/\mathrm{d}y)d/U$, where $\mathrm{d}U/\mathrm{d}y$ is the assumed constant shear of the flow. Saffman's formula (see Saffman 1965) relates the shear to the lift but fails to predict a change of sign. Saffman's lift always acts in the direction of higher fluid velocity. The change of sign has been demonstrated by Kurose & Komori (1999) and by Bagchi & Balachandar (2002). It is interesting to note that the numerical simulation by Kurose & Komori (1999) shows, for a non-rotating sphere, that the change of sign of the lift is solely due to the Reynolds number and not to the shear. (All graphs of lift versus Reynolds number plotted for different shear rates intersect at the same Reynolds number, lying close to 60 according to the cited paper.) A similar result has been reported by Bagchi & Balachandar (2002) both for non-rotating and freely rotating spheres. Their change of sign lies just higher, above $Re = 100$. The investigation of the sole effect of the shear is thus unlikely to provide a clue to the observed equilibrium of spheres transported by a pipe flow, not to mention the fact that the pure Segré–Silberberg effect relates to non-buoyant spheres having, in principle, zero slip velocity.

Alternatively, the effect of the proximity of a wall on the flow past a sphere can be investigated. The pure effect corresponds to the wake–wall interaction for a sphere moving in a quiescent fluid along a plane wall. This configuration has been investigated both experimentally and numerically. Takemura *et al.* (2002) and Takemura & Magnaudet (2003) reported experimental observations of the free ascension of bubbles along a vertical wall. Contaminated bubbles (see Takemura &

Magnaudet 2003) behave much like light rigid spheres and are thus relevant to the framework discussed. The spheres moving at velocities corresponding to Reynolds numbers ranging from 1 to 100 were observed to migrate away from the wall, indicating a repulsive lift generated by the wall proximity. This lift was found to decrease with Reynolds number and distance from the wall. Zeng, Balachandar & Fischer (2005) investigated numerically the interaction of the sphere wake with a wall. They considered both a non-rotating and and a freely rotating sphere (like Bagchi & Balachandar 2002 for shear flow) moving with constant translation velocity parallel to the wall. The investigated Reynolds numbers range from 0.5 to 300 (extending to a transitional regime characterized by an unsteady wake). They found that the lift reaches a minimum at $\sim Re = 100$ and increases again with increasing Reynolds number. Moreover, they studied the effect of the presence of the wall on the onset of unsteadiness in the wake. At distances $L > d$ (L being the distance of the centre of the sphere from the wall and d the sphere diameter) the unsteadiness sets in at a slightly lower Reynolds number than in an unconfined wake (at $Re = 270$) but, close to the wall (at $L = 0.75d$), its onset is shifted beyond $Re = 300$. The free rotation does not change the scenario qualitatively: it only tends to increase the lift coefficient slightly. To sum up, both the shear and the wake–wall interaction generate a lift tending to push the particle from the wall.

Before tackling the full problem involving both effects of the shear and of the interaction with walls in a tube, it is useful to consider that of a sphere sedimenting in a quiescent fluid in a vertical tube. This simulation was attempted by Yu, Phan-Thien & Tanner (2004). The cited work is not only of interest because it presents a fully three-dimensional simulation but also because of the transitional regimes covered. Yu *et al.* (2004) simulate the flow past a freely moving sphere by tracking the fall with the numerical mesh translated vertically with the same velocity as that of the sphere. The movement of the sphere is thus limited to the two horizontal directions. To capture this movement, a fictitious domain approach – a distributed Lagrangian multiplier (DLM) – is used on a regular fixed mesh. The flow regimes are characterized by a 'Reynolds number' equal to $\sqrt{4/3} \times G$, where G is the Galileo number used to describe the regimes of a free sphere by Jenny, Dušek & Bouchet (2004) and Veldhuis & Biesheuvel (2007):

$$G = \frac{\sqrt{|\rho_s/\rho - 1| g d^3}}{\nu}, \tag{1.1}$$

with ρ_s and ρ the solid and fluid density, g the gravitational acceleration, d the sphere diameter and ν the kinematic viscosity of the fluid. The Galileo numbers considered are 17, 87, 173, 260 and 346. They correspond to terminal Reynolds numbers, average values in unsteady regimes at the three highest G values, of 7.9, 84, 197, 300 and 400 (the last two values are difficult to estimate because the regimes are not established: see figure 3 of Yu *et al.* 2004). The solid–fluid density ratio is fixed to 1.5 (sedimenting sphere). The diameter of the tube is taken to be five times that of the sphere. The sphere is released at rest with its centre $1.25d$ from the tube wall. In the first two cases, the sphere reaches the tube axis in the radial direction and continues in a steady vertical fall. At $G = 173$, however, the trajectory is no longer plane: the sphere clearly leaves the original radial–vertical plane and the simulation captures two oscillations, possibly with decreasing amplitude, but the simulation is too short to provide a clue as to the asymptotic state. At the two highest Galileo numbers, the trajectories become close to helical (about three times the pitch is captured) and the wake visualization exhibits vortex shedding. Of course, computational cost prevented

the authors from investigating the asymptotic regimes. It is, nevertheless, clear that the latter are unlikely to be inferred directly from what is known about the transitional regimes of an unconfined freely falling sphere. Indeed, the most striking facts are that the observed periodicity is not related to the vortex shedding (it sets in earlier and has a significantly longer vertical length scale) and that the trajectory is not plane.

The simulations discussed are not long enough to provide reliable information on developed asymptotic regimes, nor is the parametric study sufficiently fine to indicate likely bifurcations responsible for the asymptotic dynamics. The aim of the present paper is to provide more complete and more accurate data. For this purpose we have developed a computationally more efficient method of simulating the investigated configuration, which allows us to obtain a refined resolution of boundary layers without using a dynamic meshing, such as that in the arbitrary Lagrangian Eulerian (ALE) approaches. The mathematical formulation and numerical method are briefly presented in § 2. The results are presented in the following three sections. We found that, very early on, the regimes of the fall of the sphere in a tube become chaotic. The ordered, early stages of the transition are described in § 3. The vortex shedding is observed to set in later, in the chaotic stages of the transition, to which we dedicate §§ 4 and 5.

2. Mathematical formulation and numerical method

We solve the incompressible Navier–Stokes equations in a cylindrical domain filled with a fluid of uniform density ρ and kinematic viscosity ν containing a homogeneous moving sphere of diameter d and density ρ_s. A sedimenting sphere ($\rho_s > \rho$) is considered to move freely in a quiescent fluid. The geometry is represented in figure 1. The tube is simulated by a cylindrical domain of diameter $D = 5d$. The sphere's centre is in a horizontal plane situated $15d$ downstream of the inflow (the bottom cylinder basis) and $20d$ upstream of the outflow (i.e. the overall cylinder height is $35d$). To represent the moving geometry, we embed the sphere in a spherical subdomain moving in a horizontal plane in a translation motion with the horizontal velocity of the sphere movement. The remaining four degrees of freedom of the sphere are accounted for by boundary conditions. The vertical translation velocity is imposed as a Dirichlet boundary condition on the outer cylinder wall. The angular velocity of rotation is taken into account by the Dirichlet boundary conditions of the velocity field at the solid sphere surface in the spherical subdomain. In accordance with Jenny *et al.* (2004) we non-dimensionalize the velocity by the velocity scale defined by the effective acceleration and the sphere diameter $v_{unit} = \sqrt{(1 - \rho_s/\rho)gd}$, and we express the velocity field with respect to a fixed reference frame. The length scale of non-dimensionalization is defined by the sphere diameter. Non-dimensionalized quantities based on these velocity and length scales are used throughout the paper. The non-dimensionalized flow equations read as follows:

$$\frac{\partial \boldsymbol{v}}{\partial t} + [(\boldsymbol{v} - \boldsymbol{u}_{mesh}) \cdot \nabla \cdot]\boldsymbol{v} = -\nabla p + \frac{1}{G}\nabla^2 \cdot \boldsymbol{v}, \tag{2.1}$$

$$\nabla \cdot \boldsymbol{v} = 0, \tag{2.2}$$

where G is the Galileo number defined in (1.1) and $\boldsymbol{u}_{mesh}$ is the mesh velocity equal to the sphere translation velocity $\boldsymbol{u}$ in the spherical subdomain and only to its vertical projection in the cylindrical one. The translation and angular velocity of the sphere

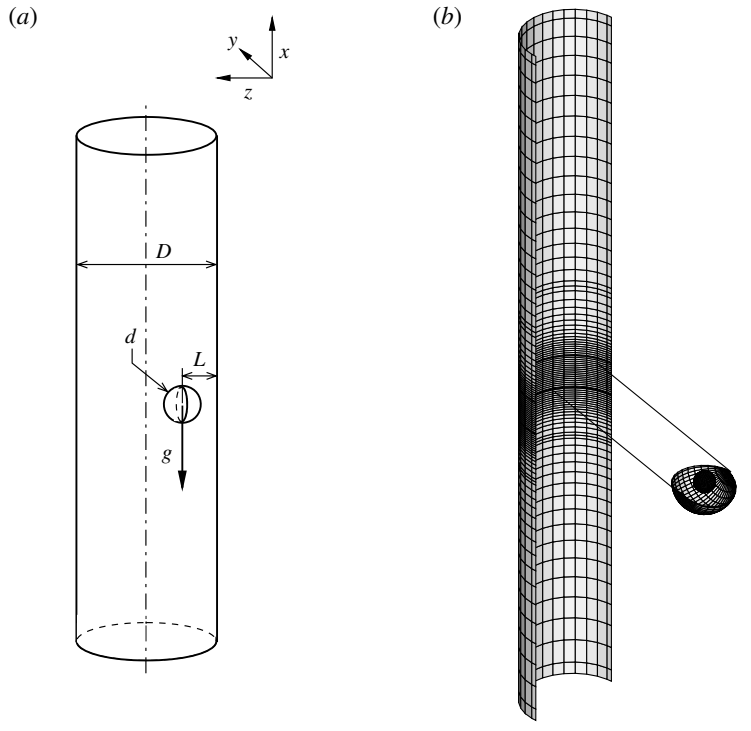

FIGURE 1. (*a*) Diagram of the configuration: d is the sphere diameter, D is the tube diameter, g is gravity, L is the distance of the sphere centre from the tube wall. (*b*) Meshes of the cylindrical and spherical subdomains.

($\boldsymbol{u}$ and $\boldsymbol{\Omega}$) obey the motion equations (see Jenny & Dušek 2004)

$$\frac{\rho_s}{\rho}\frac{\mathrm{d}\boldsymbol{u}}{\mathrm{d}t} = \frac{6}{\pi}\boldsymbol{F}_{fl}(\boldsymbol{v}, p) - \boldsymbol{i}, \tag{2.3}$$

$$\frac{\rho_s}{\rho}\frac{\mathrm{d}\boldsymbol{\Omega}}{\mathrm{d}t} = \frac{60}{\pi}\boldsymbol{M}_{fl}(\boldsymbol{v}, p), \tag{2.4}$$

where $\boldsymbol{i}$ is the vertical upward pointing unit vector and $\boldsymbol{F}_{fl}$ and $\boldsymbol{M}_{fl}$ are the hydrodynamic force and torque.

Since it is necessary to simulate a non-axisymmetric geometry, the spectral approach used in Jenny *et al.* (2004) and Jenny & Dušek (2004) is no longer applicable. Equations (2.1)–(2.4) are thus solved by the parallel Navier–Stokes multi-block (NSMB) solver (see Vos *et al.* 2002) based on a finite volume discretization. The moving geometry was obtained by implementing the chimera method (see Deloze, Hoarau & Dušek 2010 for more details) within the NSMB code. The NSMB solver was originally a compressible code, used for the present purpose in the incompressible limit obtained by artificial preconditioning of Chorin (1968): the density is fixed and the time derivative of the density appearing in the compressible version of the continuity equation is replaced by the artificial compressibility term $\partial p/\partial\tau$, where τ is an internal time-stepping variable. Within each physical time step, an inner convergence to a limit pressure value is reached, making the artificial compressibility term vanish. The incompressibility constraint (2.2) is thus satisfied. The principle

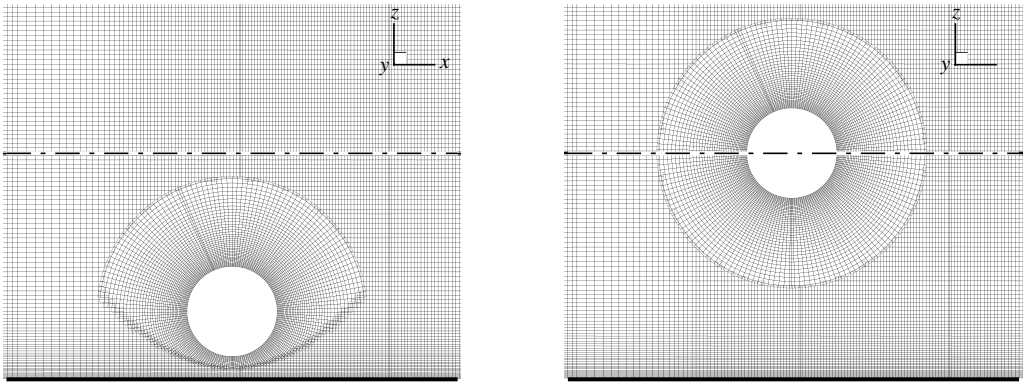

FIGURE 2. Cross-section of the chimera overlapping taken in the plane defined by the sphere centre and the tube axis. The two figures illustrate the adaptation of the mesh to moving geometry.

of the chimera subdomain interconnection resides in using only a limited layer of overlapped cells required by the stencil of the used (second-order) discretization and in discarding, dynamically, unused cells (see figure 2). The diameter of the moving spherical subdomain has been chosen equal to $3d$.

The numerical method has been tested by comparing the thresholds of the primary and secondary bifurcations in the wake of a sphere translating with a uniform velocity along the tube axis. The latter were determined using the spectral–spectral-element method of Ghidersa & Dušek (2000) and the adapted NSMB code for the confinement $D/d = 5$ with a total of 1.6 million mesh points in the spherical and cylindrical subdomains. For the threshold of the primary bifurcation, the NSMB code yields approximately $Re_{crit} = 210$ as compared to 212 obtained by the spectral–spectral-element method. For the threshold of the secondary bifurcation the values are 279 and 273, respectively. The drag and lift were also compared. At $Re = 200$ the NSMB code and the spectral–spectral-element code yield $C_D = 0.8334$ and 0.8240, respectively (1.2 % difference); at $Re = 300$ the corresponding values are 0.7101 and 0.7038 (0.9 % difference). The comparison of the lift coefficient is represented graphically in figure 3. The largest discrepancy concerns mean values obtained in the unsteady periodic regime at $Re = 300$. It represents 0.7 % of the value of the drag coefficient. (The absolute value of the discrepancy must be related to the value of the drag coefficient and not to that of the lift coefficient, varying from zero at the onset of the axisymmetry breaking.) Moreover, amplitude of the lift (and drag) oscillation is relatively well captured (with the same relative precision based on the drag coefficient value).

The mesh independence was tested on eight meshes, with increasing refinement going from 0.7 to 6.7 million mesh points. The chosen configuration was that of a sphere moving with uniform velocity and with its centre placed at a fixed distance $L = d$ from the tube wall at $Re = 200$. The proximity of the wall generates a constant non-zero lift, which was computed along with the drag. Both components of the hydrodynamic force are represented in figure 4 as a function of the mesh refinement. It is seen that the drag coefficient varies by less than 1 % for all considered refinements. The lift coefficient varies relatively strongly for the three coarsest meshes, but starting

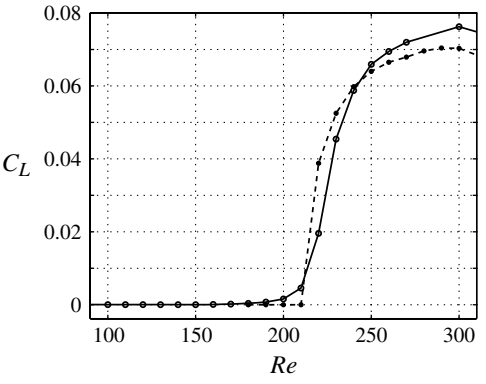

FIGURE 3. Lift as a function of the Reynolds number for a sphere fixed at the axis of a tube of diameter $5D$. Solid line, results obtained by the modified NSMB code; dashed line, results obtained by the code of Ghidersa & Dušek (2000). Beyond the secondary instability threshold at $Re = 275$, mean lift is represented.

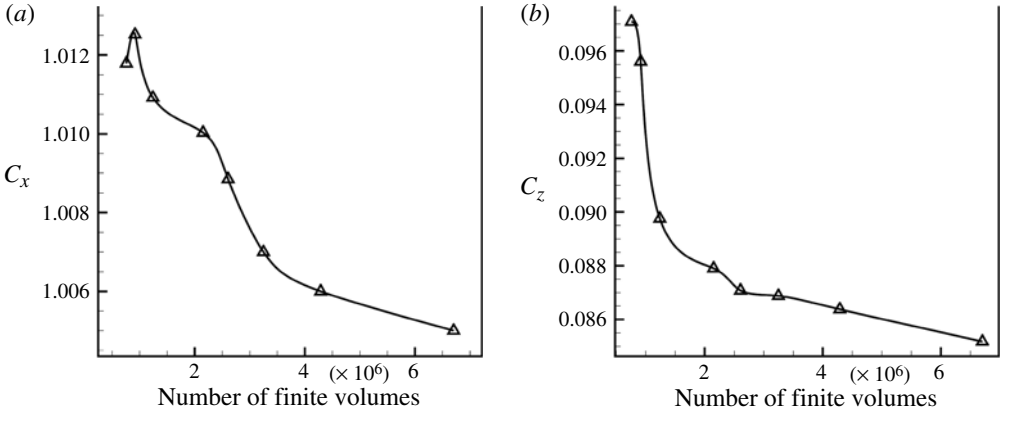

FIGURE 4. (*a*) Drag coefficient and (*b*) lift coefficient of a sphere placed in a tube of diameter $D = d$, with its centre lying at a distance of d from the tube wall and moving parallel to the tube axis at a velocity corresponding the the Reynolds number of 200 as a function of the number of mesh points.

from the mesh with 1.6 million mesh points the variation becomes moderate, and represents less than 0.4 % of the drag coefficient.

As shown by tests of mesh independence, the results can be improved if more mesh points are used, but very long runs are needed to capture the asymptotic regimes of the transition scenario. This explains the chosen compromise. Moreover, the discretization does not respect the axisymmetry of the configuration where the sphere is placed exactly at the tube axis as perfectly as the spectral one. The cylindrical subdomain is split into eight blocks and the spherical one into four blocks. This splitting brings about a small but not entirely negligible perturbation of the transitional regimes. In particular, it introduces a slight non-axisymmetry resulting in an unsharp threshold of axisymmetry breaking (see figure 3), and probably explains why the planar symmetry expected above the primary instability threshold is imperfect and why

the orientation of the symmetry plane is not arbitrary. Let us, however, remark that similar imperfections are encountered in experiments.

The time discretization is entirely implicit except for the motion equations. The overwhelming majority of simulations of sedimenting particles treats the motion equations in an explicit way. A weak formulation enables a combined fluid–solid formulation (see e.g. Glowinski *et al.* 2001; Hu, Patankar & Zhu 2001), which can serve as the basis of a strong fluid-coupling, consisting in inverting a complete matrix including the fluid and solid degrees of freedom, or various operator splitting methods can be used to simplify the matrix inversion. Hu *et al.* (2001) remark that a fully explicit treatment of the solid body degrees of freedom decouples the fluid equations from the solid body ones. At the same time, they show that the explicit treatment becomes unstable when the mass of the solid body becomes smaller than its added mass. Therefore, only rising spherical particles need a more sophisticated treatment, as shown in Jenny *et al.* (2004). In the present case, the computing costs limit the feasibility of the parametric study to the variation of just a single parameter (the Galileo number) out of the three present (G, ρ_s/ρ and D/d). We select the case of $\rho_s/\rho = 2$, for which the simple explicit approach presents no problem. The same approach to the treatment of the solid–fluid interaction is used whenever the added mass permits stability (see also Uhlmann 2005; Borazjani, Ge & Sotiropoulos 2008). The overall time-discretization accuracy was tested by considering time steps $\Delta t = 0.015$ and 0.003. For the fixed sphere at $Re = 300$ this time step refinement brings about a variation of only 3×10^{-4} of the amplitude of oscillation of the lift coefficient. Roughly the same insensitivity to the time step was found in the configuration of the freely moving sphere involving the (weak) coupling with the motion (2.3) and (2.4). The shorter time step was retained to produce the results. The high accuracy obtained is explained by the large physical scales of the simulated system (see below).

The efficiency of the numerical implementation described is relatively satisfactory for this type of three-dimensional problem. Nevertheless, the fully three-dimensional mesh typically requires two months of parallel computation on 12 cores for a full investigation of a single Galileo number value in a chaotic regime.

3. Early stages of transition, $G < 180$

As already stated in the previous section, the costs of a full investigation of the space of all the three parameters, G, ρ_s/ρ and D, are not acceptable. As the Galileo number is expected to be the most relevant parameter, we fix the diameter ratio to 5 ($D/d = 5$) to keep the same geometry as Zeng *et al.* (2005) and we take a constant density ratio $\rho_s/\rho = 2$. Exceptionally, at $G = 250$, we investigate the effect of increasing density by also considering $\rho_s/\rho = 3$ and 5. The Galileo number sweeps the interval from 50 to 350.

In the laminar regimes, at sufficiently low Galileo numbers, the sphere behaves in agreement with expectations based on the knowledge of the lift direction acting on a sphere close to a wall (see Takemura & Magnaudet 2003; Zeng *et al.* 2005). The lift being repulsive (see Takemura & Magnaudet 2003; Zeng *et al.* 2005), a sphere abandoned without initial velocity off the tube axis will accelerate in the vertical and radial directions and will thus be expected to follow a plane trajectory in the radial–axial plane defined by its initial position. Asymptotically, the trajectory will reach the tube axis where the lift will become zero. The final state will be free fall with a terminal velocity for which the drag compensates gravity and buoyancy. This

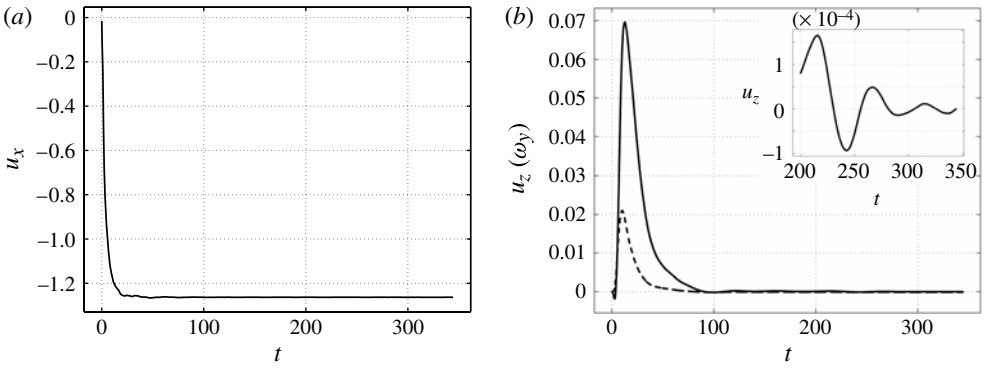

FIGURE 5. Non-dimensionalized (*a*) vertical (u_x) and (*b*) horizontal (u_z) components of the sphere velocity as functions of time t at $G = 150$. The dashed line in (*b*) represents the angular velocity.

result was, indeed, obtained at $G = 50$, 100 and 150. The terminal velocity corresponds to Reynolds numbers 42, 110 and 190, respectively. In figure 5 the velocity transients of a sphere released at rest, with its centre positioned $1.5d$ off the tube axis (i.e. $1d$ from the wall), are represented in the case of $G = 150$. The initial deviation is taken along the z-axis, i.e. $z(0) = 1.5d$ and $y(0) = 0$. (The x axis is vertical.) The vertical acceleration ramp corresponds to ∼30 time units (equal to $\sqrt{d/(|\rho_s/\rho - 1|g)}$), after which the sphere settles into its terminal velocity (see figure 5*a*). The radial velocity (figure 5*b*) rapidly (within 13 time units) reaches a maximum corresponding to more than 5.5 % of the terminal velocity. Then it decreases almost monotonically to zero as the sphere settles into the flow axis. The decay is monotonic only at $G = 50$ and 100. At $G = 150$ decaying oscillations appear in the final stage of convergence as a precursor sign of a Hopf bifurcation (see inset of figure 5*b*). Numerical imperfections induce a non-zero perpendicular velocity component u_y which, however, remains significantly smaller than the u_z velocity component. (The u_y velocity component reaches a peak of acceleration similar to u_z. The value of the maximum represents ∼2 % of the peak of u_z.) This yields an almost perfectly straight and radial projection of the trajectory onto a horizontal plane. The presence of a primary Hopf bifurcation contrasts with the regular bifurcation exhibited for an unconfined sphere. In figure 5*b* we also plotted the angular velocity accompanying the settling into the vertical fall along the tube axis. It is perpendicular to the plane of the trajectory and roughly copies the evolution of the horizontal velocity. This behaviour of angular velocity is found up to the chaotic regime.

At $G = 160$ we are already in the presence of a supercritical regime. An additional computation at $G = 155$ shows that the threshold of the bifurcation lies between $G = 155$ and $G = 160$. Figure 6 represents the settling into the asymptotic regime starting from two different initial conditions: the end of the already described simulation at $G = 150$ and the established solution at $G = 170$ (figure 9*c*,*d*). The development of the instability from the vertical regime at $G = 150$ represented in figure 6(*a*) is typical for a Hopf bifurcation. The asymptotic regime obtained is perfectly periodic with period $T = 67.12$ expressed in time units $\sqrt{d/(1 - \rho_s/\rho)g}$. As the average terminal velocity is $\overline{v_x} = 1.287$, this corresponds to a (mean) Strouhal number $St = 0.0116$. Note that the oscillations of angular velocity (the dashed line in figure 6*a*) are in phase with those of the horizontal velocity.

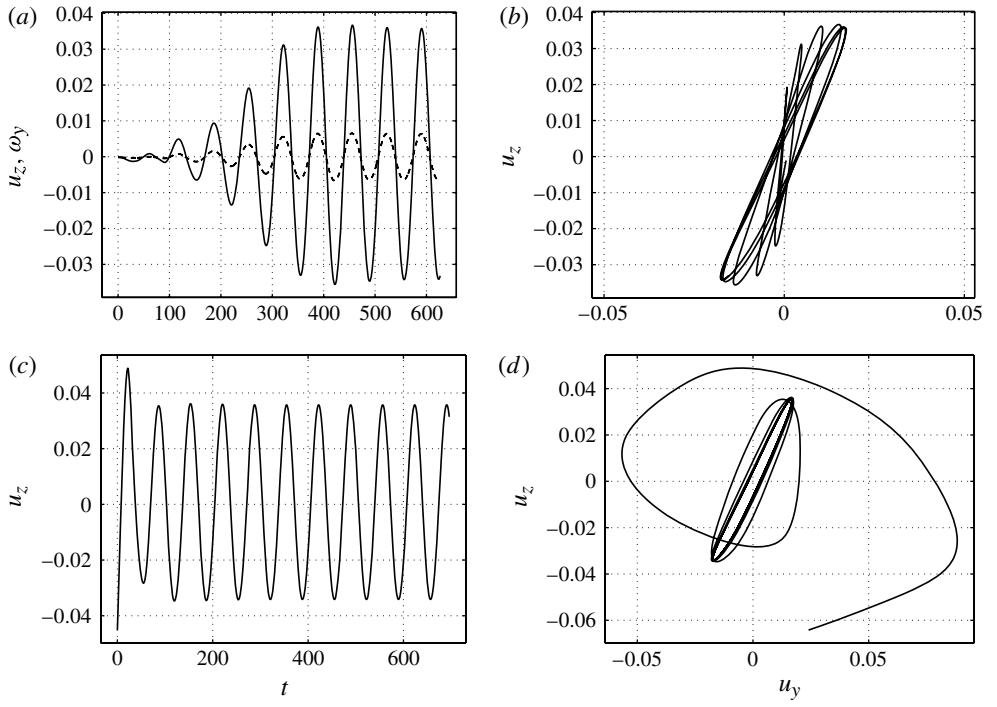

FIGURE 6. $G = 160$. (*a*) The z-component of the horizontal velocity as a function of time. (The dashed line represents the y-component of angular velocity.) (*b*) The curve described by the horizontal velocity components. The starting point (visible close to the origin) corresponds to $t = 250$ in (*a*). (*c,d*) The same but with an initial condition taken from a simulation at $G = 170$.

The Hopf bifurcation breaks the original (theoretically perfect) axisymmetry of the steady vertical fall. Simple theoretical considerations (see Danaila, Dušek & Anselmet 1998) show that the instability generates two helical modes of opposite helicity corresponding to the unstable ($\gamma > 0$) complex eigenpair $\gamma \pm \mathrm{i}\omega$. A flow field of this form generates a non-zero lift and, by the same token, a non-zero horizontal velocity that can be represented as a complex function of time (see Jenny & Dušek 2004) $u_+ = u_y + \mathrm{i}u_z$ expressed by two complex amplitudes $A_\pm$:

$$u_+ = A_+(t)\mathrm{e}^{\mathrm{i}\omega t} + A_-(t)\mathrm{e}^{-\mathrm{i}\omega t}. \tag{3.1}$$

A weakly nonlinear third-order approximation of the dynamics of the axisymmetry breaking by a Hopf bifurcation yields the following equations (Danaila *et al.* 1998):

$$\frac{\mathrm{d}A_\pm}{\mathrm{d}t} = [\gamma - (C\,|A_\pm|^2 + D\,|A_\mp|^2)]A_\pm. \tag{3.2}$$

Here C and D are complex constants, the same in both equations, with upper and lower sign to account for the symmetry with respect to the change of the sign of helicity. A simple calculation shows that equations (3.2) have two types of asymptotic solution:

(i) one of $|A_+|$ or $|A_-|$ zero, the other equal to $(\gamma/C_r)^{-1/2}$;
(ii) both modules equal and $|A_+| = |A_-| = [\gamma/(C_r + D_r)]^{-1/2}$.

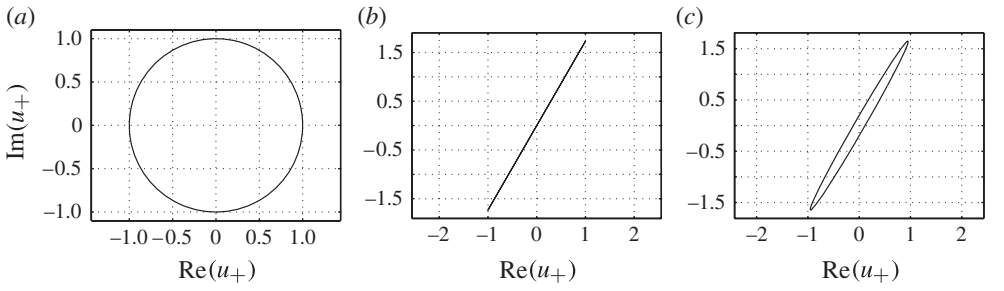

FIGURE 7. Paths in the complex plane of the modelled complex velocity of (3.3) for (*a*) a single non-zero amplitude, $A_{-,\infty} = 0$, (*b*) two equal amplitudes $|A_{+,\infty}| = |A_{-,\infty}|$, (*c*) $|A_{-,\infty}| = 0.9|A_{+,\infty}|$.

(Here C_r and D_r stand for the real parts of C and D. Both C_r and D_r are assumed to be positive.) For $C_r < D_r$ the solution (i) is stable and (ii) is unstable. The converse is true for $D_r < C_r$. The imaginary parts of C and D yield a nonlinear shift of angular frequency. As a result, (3.1) yields the asymptotic states

$$u_{+,\infty} = [|A_{+,\infty}|e^{i(\omega' t-\varphi_+)} + |A_{-,\infty}|e^{-i(\omega' t-\varphi_-)}] \tag{3.3}$$

where $\omega' = \omega + \Delta\omega$ is the angular frequency of the limit cycle and $\varphi_\pm$ phase shifts determined by the initial perturbation. The trajectory in the complex plane in case (i) is a circle and in case (ii) a straight line, the inclination of which is given by the phase shifts, i.e. by initial conditions. Let us note that an imperfect axisymmetry of the base flow yields different constants for upper and lower signs in (3.2). This results in unequal amplitudes $|A_{+,\infty}| \neq |A_{-,\infty}|$, yielding a flat ellipse instead of a straight line (see figure 7).

The results of the simulation represented in figure 6 are quite close to the case of two equal amplitudes, the flat ellipse being attributable to imperfections of the code. The latter also tends to orient the main axis of the ellipse in the same direction whatever the initial condition, as can be seen in figure 6(*b,d*), the second simulation starting from a different initial condition, taken from a computation at a higher Galileo number ($G = 170$). The state is thus (almost) symmetric with a symmetry plane oriented in the direction of the flat ellipse. This also holds for the wake structure represented in figure 8(*a*).

The asymptotic state at $G = 160$ contrasts with that reached only 5 units of G higher, at $G = 165$. The initial condition was taken to be the same as in figure 6(*c,d*), i.e. from a simulation at $G = 170$. Again a periodic asymptotic state is reached (see figure 9). Its period is a little shorter than at $G = 160$: 64.5. The corresponding Strouhal number is 0.012 (for an average vertical velocity of 1.29). The most striking feature is that the path of the horizontal projection of the velocity is no longer a flat ellipse but a nearly circular cycle (deformed by higher-order harmonics). The same shape is obtained at the higher Galileo number of 170. The switching from the flat ellipse to the circular shape can be attributed to a bifurcation changing the stability of the two alternative states arising at an axisymmetry-breaking Hopf bifurcation. An additional check, consisting in running a simulation at $G = 160$ starting for the established state at $G = 165$ and, conversely, at $G = 165$ starting from $G = 160$, confirms that this bifurcation is supercritical, that there is no bistability between these states, and that the bifurcation threshold indeed lies between $G = 160$ and $G = 165$.

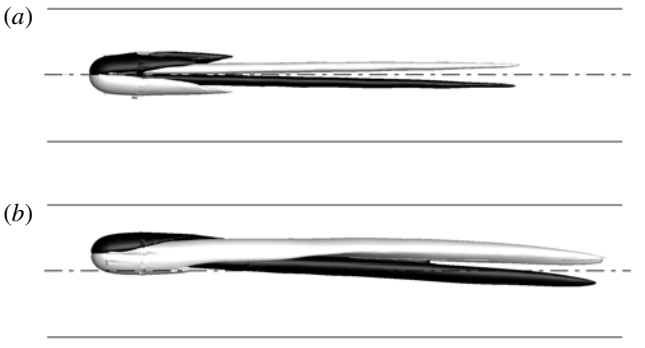

FIGURE 8. Iso-surfaces of the vertical vorticity in the wake of the sphere at (*a*) $G = 160$, (*b*) $G = 170$. Iso-vorticity levels: (*a*) ± 0.02, (*b*) ± 0.05.

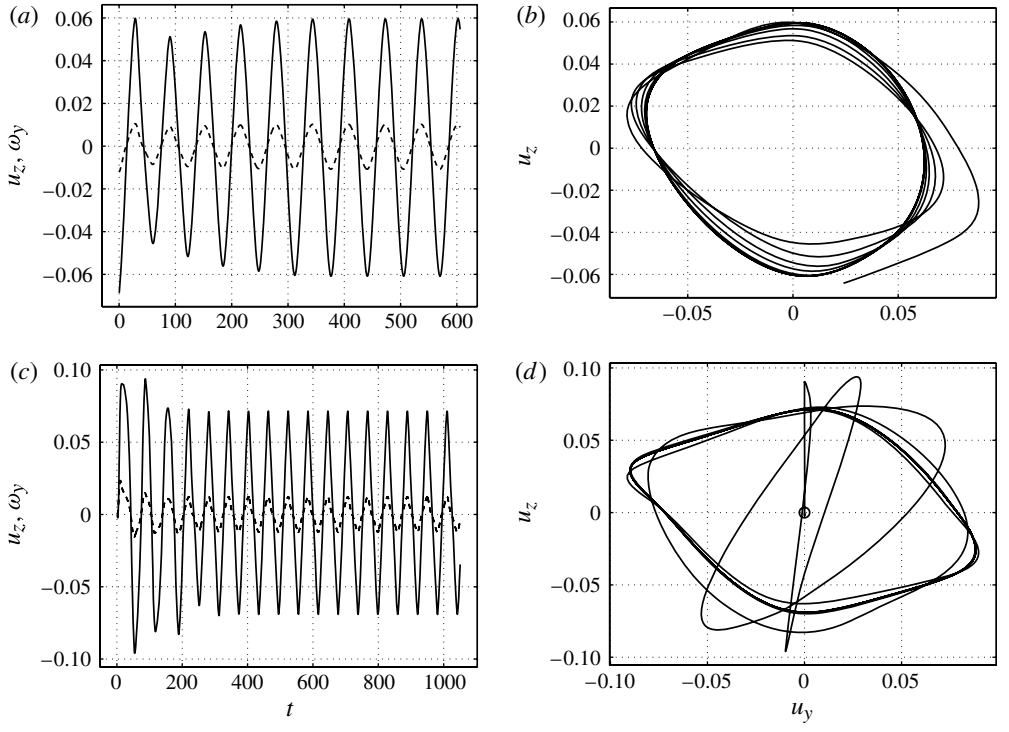

FIGURE 9. (*a*) The z-component of the horizontal velocity (solid line) and the y-component of the angular velocity as a function of time, (*b*) The curve described by the horizontal velocity components at $G = 165$. (Initial condition: asymptotic solution at $G = 170$.) (*c*,*d*). The same at $G = 170$ with initial condition (circle in *d*) corresponding to a vertical fall. The dashed lines in (*a*) and (*c*) represent the corresponding perpendicular component of angular velocity.

For each of these states, the wake structure remains qualitatively the same (see figure 8), similar to that of the steady oblique state of an unconfined sphere (see Jenny *et al.* 2004) or the steady non-axisymmetric state of an unconfined and unheated

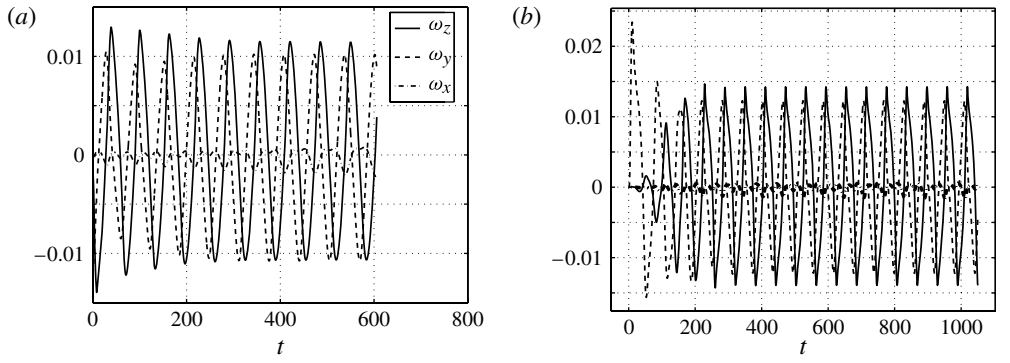

FIGURE 10. (*a*) Angular velocity components at $G = 165$. (*b*) The same angular velocity components at $G = 170$.

fixed sphere (see Kotouč, Bouchet & Dušek 2009). Note, however, the twist of the wake at $G = 170$ related to the helical trajectory. In contrast, at $G = 160$, the wake has a planar symmetry. The simulation at $G = 170$ shows asymptotic states similar to that at $G = 165$ (see figure 9*c,d*). The trajectory smooths the oscillations of the magnitude of the horizontal velocity vector and is quite close to helical. Let us note, for further discussion, that the frequency of the oscillations at $G = 170$ is 0.0164 in our units, i.e. if the vertical asymptotic mean velocity of 1.295 is taken into account, the Strouhal number is equal to 0.0127.

The horizontal angular velocity components remain in phase with the corresponding (perpendicular) horizontal velocity components. In figure 10 it can be seen that the rotation with respect to the vertical axis is practically non-existent, and that the oscillations of the horizontal components have a phase shift close to $\pi/2$. A plot of ω_z versus ω_y features a cycle very similar to that of u_z versus u_y. To sum up, even on the helical trajectory, the sphere rotates in the local trajectory plane (defined by the vertical direction and the velocity vector). The modulus of the rotation velocity is $\sim$5 times smaller than that of the horizontal one in our non-dimensional units.

4. Chaotic states

The periodic state loses its stability between $G = 170$ and 180. A simulation started at the end of the run represented in figure 9(*c,d*) shows non-periodic behaviour (see figure 12). At $G = 200$, the limit cycle represented by the path of the horizontal velocity vector is already well destabilized, resulting in a disordered trajectory. Figure 13 represents the results of a simulation at $G = 200$ in which the sphere has again been released from rest at $1.5d$ from the tube axis in the xz vertical plane. The disordered horizontal projections of the path of the velocity vector and of the trajectory itself are represented in figures 13(*c*) and 13(*d*), respectively. It is clearly seen that what makes the difference from the ordered states of the previous section is the more complex and non-periodic time-dependence of the horizontal velocity components (compare figures 9*c* and 13*b*). This feature is related to intermittent additional oscillations appearing when the u_z velocity component is close to zero and the u_y velocity is close to the maximum of its amplitude. In figure 14(*a,c*), it is clearly seen that these oscillations arise at the moment when the sphere is situated closest to the tube axis. A rough estimate of the period of these new oscillations (see the

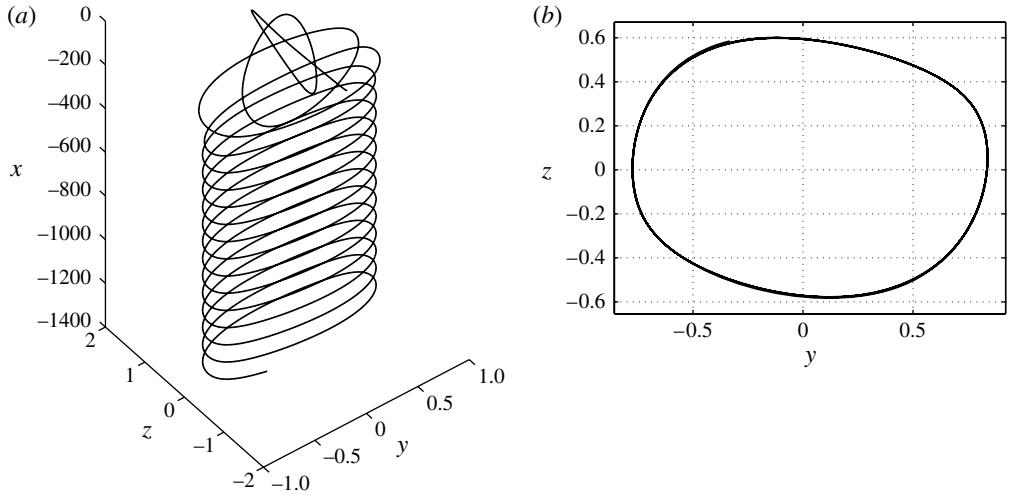

FIGURE 11. A three-dimensional representation and the horizontal projection of the trajectory at $G = 170$.

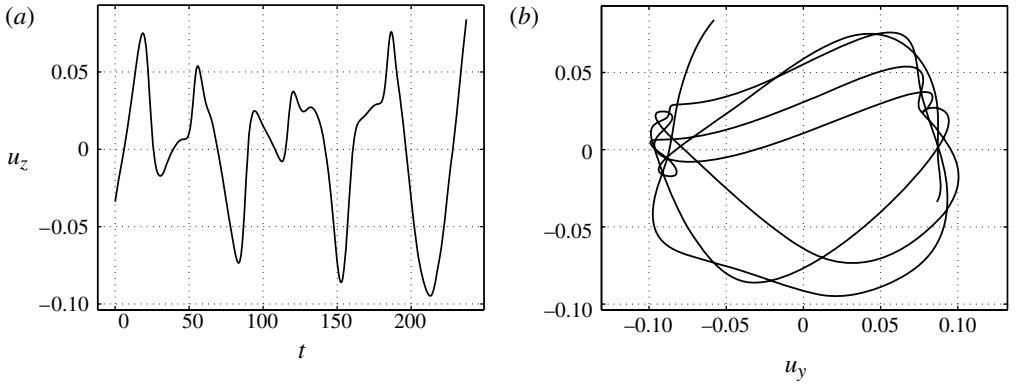

FIGURE 12. $G = 180$. (*a*) The z-component of the horizontal velocity as a function of time. (*b*) The path of the horizontal velocity vector. Run restarted from the end of the simulation at $G = 170$.

leftmost maximum or the rightmost minimum in the upper graph of figure 14(*a*) is ∼10. This is confirmed by the Fourier transform plotted in figure 14(*d*). The dominant peak (marked f_1) corresponds to the frequency of 0.018 related to the dominant helical motion due to the wake–wall interaction. It is indeed comparable to the value of 0.0164 seen at $G = 170$. The Fourier transform contains two further peaks at 0.054 and 0.085. The latter correspond to the third and fifth harmonic. In contrast, the peak marked f_2 corresponds to a frequency of 0.099, equal to 5.5 times f_1 (i.e. no integer multiple) and yields, moreover, an oscillation period of 10 in agreement with that appearing at the extrema of the v_y velocity. The oscillation of the horizontal velocity

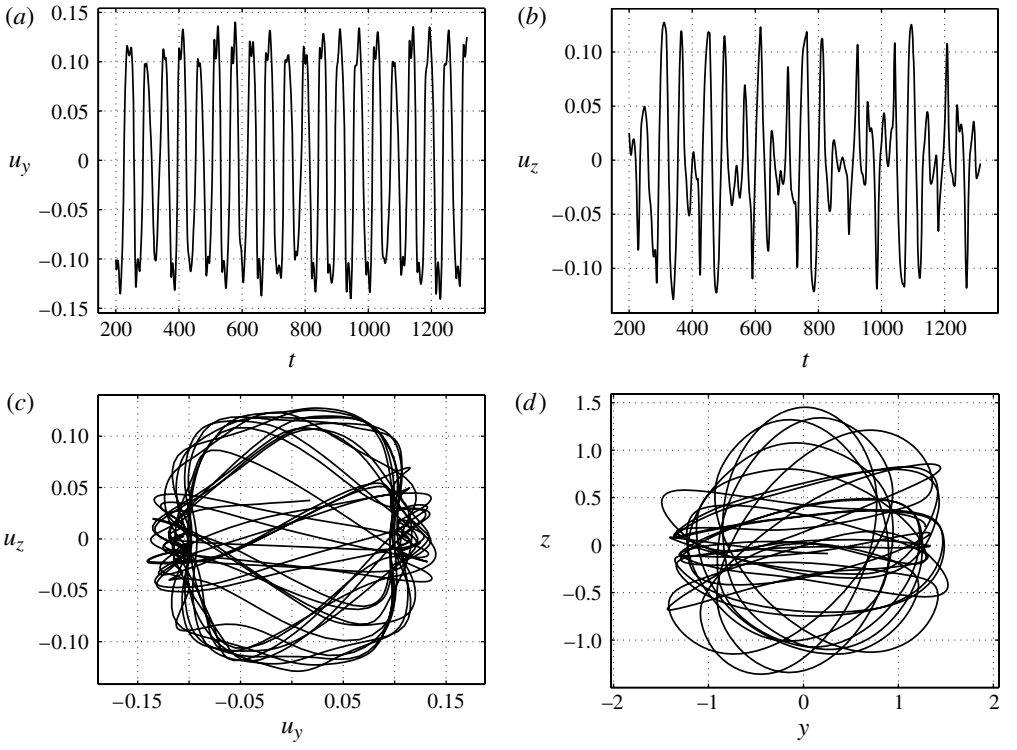

FIGURE 13. $G = 200$. (*a*) The *y*-component of the horizontal velocity as a function of time. (*b*) The *z*-component of the horizontal velocity as a function of time. (*c*) The path of the horizontal velocity vector. (*d*) Horizontal projection of the trajectory. Run started with the sphere at rest. The first 200 time units of transients have been truncated.

components is quite well copied by the perpendicular components of the angular velocity. Both reflect the same dynamics.

The frequency equal to 0.1 ($St = 0.075$, the average vertical velocity being 1.32) is comparable to that of the oblique oscillating state of an unconfined freely falling sphere reported in Jenny *et al.* (2004) to be 0.075 for the present density ratio of 2 and a similar Galileo number. The oscillating state was shown in the same paper to be related to the onset of vortex shedding. Indeed, in figure 15, the vortex shedding appears at $G = 180$, at the same time as the chaotic time behaviour at $G = 180$. Figure 15(*a*) also contrasts with figure 8(*b*). This indicates that the new chaotic state is mainly due to the onset of vortex shedding.

A second, even if incommensurable, frequency does not yet explain the chaotic behaviour. How the chaotic trajectory arises can be understood from the sequence of snapshots of the wake structures in figure 16 obtained using the λ_2 iso-surfaces suggested by Jeong & Hussain (1995). The snapshots cover a little more than one half-period of the slow oscillation. It can be seen that at moments when the sphere approaches the wall the vortex shedding disappears, and then it develops again when it comes close to the tube axis. Such wake extinction is already visible in figure 15(*a*), where the near wake does not instantaneously present fine vortical structures visible farther downstream. The redevelopment of the wake after its extinction introduces a third, slow, time scale: the inverse of the amplification rate of the instability. This

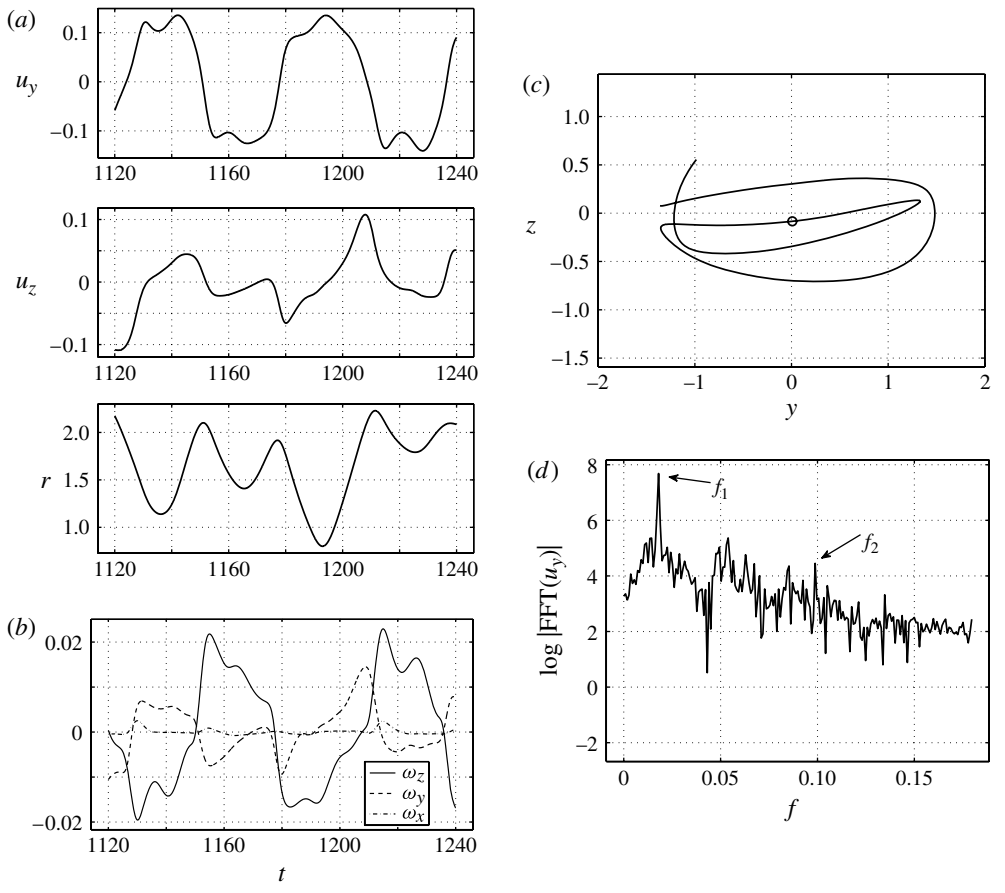

FIGURE 14. $G = 200$. (*a,b,c*) Close-up of the time interval $114 < t < 126$ of figure 13. (*a*) Top to bottom: y- and z-components of the horizontal velocity, and the distance from the tube axis. (*b*) The angular velocity components. (*c*) The trajectory (the circle marks the point at $t = 1193$ where the trajectory is closest to the tube axis). (*d*) Fourier transform of the u_y velocity in figure 13(*a*). $f_1 = 0.018, f_2 = 0.099$.

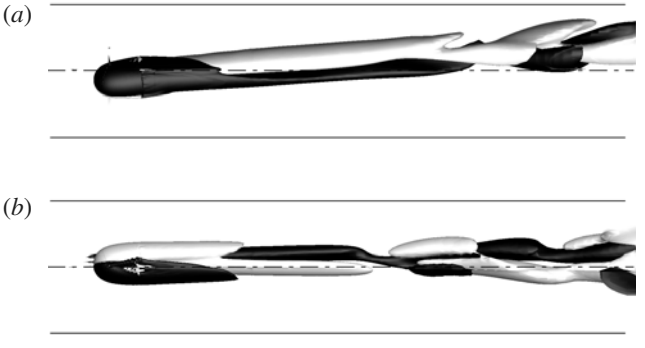

FIGURE 15. Iso-surfaces of the vertical vorticity in the wake of the sphere at (*a*) $G = 180$ and (*b*) $G = 200$. Iso-vorticity levels ± 0.05 in both figures.

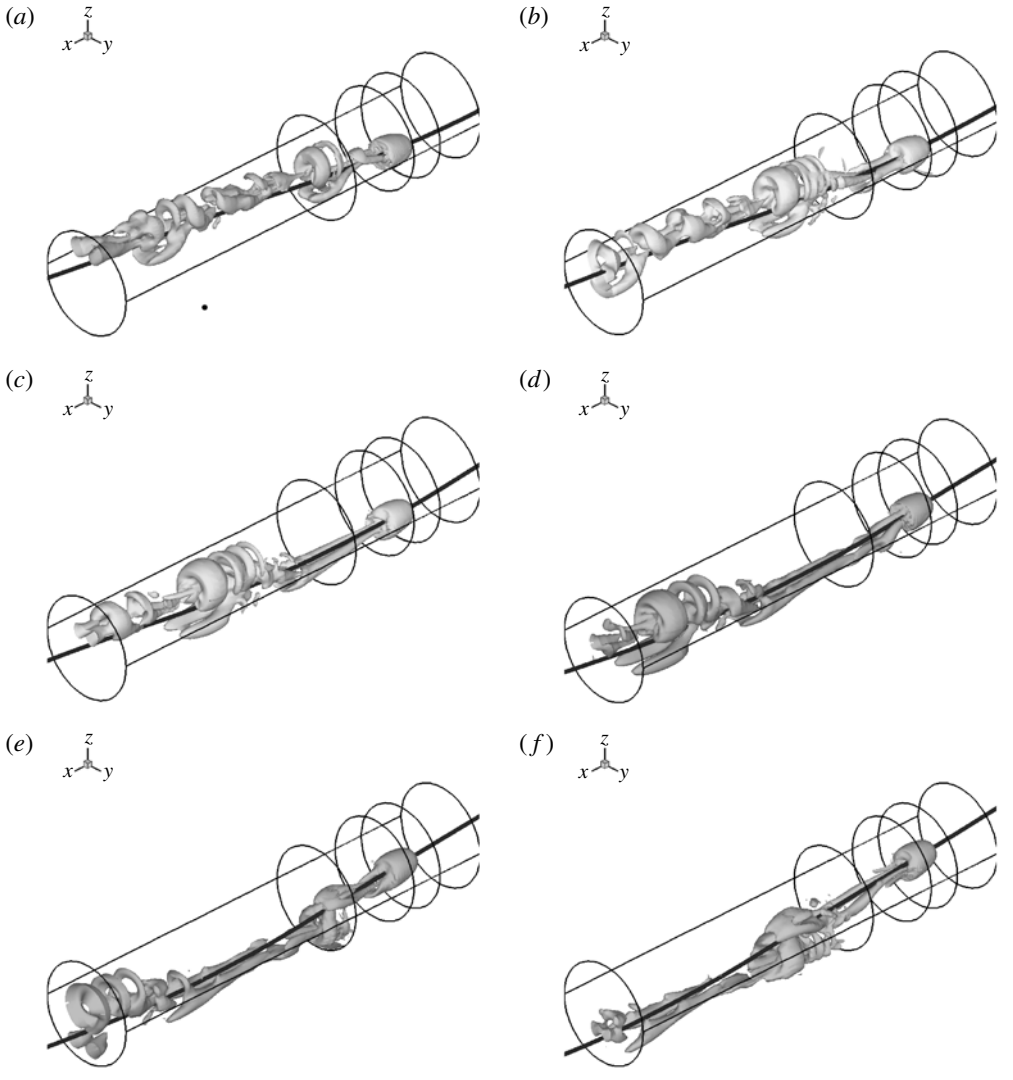

FIGURE 16. Extinction of the vortex shedding close to the wall and its redevelopment at the tube axis. The time interval between two snapshots is 6.3 time units, the whole sequence spanning over 31 time units. The thick dark line marks the trajectory of the sphere's centre and the circles mark the position of the tube walls. Supplementary movie available at http://dx.doi.org/10.1017/jfm.2012.362.

occurs whenever intermittency is responsible for the onset of chaos (see e.g. the Lorentz model).

5. Effect of higher density at $G = 250$

A significant and sudden increase of frequency of the oblique oscillating regime of a freely falling sphere was noted by Jenny *et al.* (2004) when the solid–fluid density ratio was varied from 2 to 3. For this reason, we investigated the cases

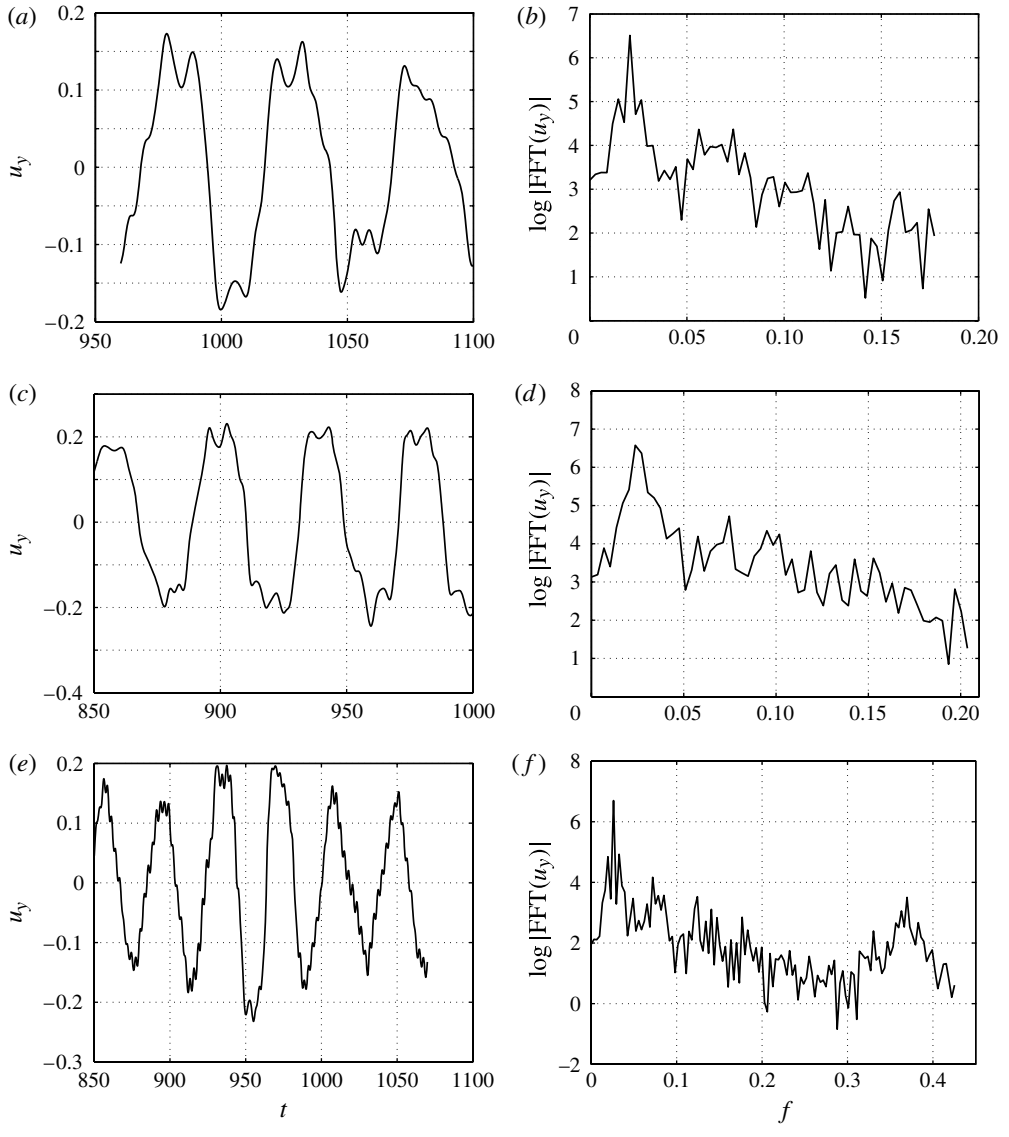

FIGURE 17. $G = 250$. (*a,c,e*) Close-ups of u_y versus time graphs. (*b,d,f*) Fourier transforms: first line, $\rho_s/\rho = 2$; second line, $\rho_s/\rho = 3$; third line, $\rho_s/\rho = 5$.

of $\rho_s/\rho = 3$ and 5. The case of the Galileo number of 250, at which the vortex shedding is fully developed, was chosen for the purpose. As shown in figure 17, the frequency of wall–wake interaction grows only slightly from ∼0.021 to 0.025 (the main peak in the graphs of Fourier transforms and the principal period in the u_y versus t graphs). There is little difference in the vortex shedding frequency and intensity between $\rho_s/\rho = 2$ and 3. The peak identified at $G = 200$ as corresponding to the vortex shedding frequency cannot be discerned. It most likely disappears in the broad peak of the fifth harmonic of the principal frequency. A significant change appears when the density ratio is increased to 5. A strong peak at the frequency of ∼0.36 appears in the Fourier transform in figure 17(*f*). This frequency corresponds to the

rapid oscillations in the figure 17(*e*). The change in vortex shedding probably appears at a higher density ratio than for an unconfined sphere, and the new frequency is also much higher in the confined configuration.

6. Conclusion and discussion

The present paper shows that the transition scenario of the freely falling sphere confined in a tube is qualitatively totally different from that of an unconfined sphere. Nonetheless, a definite link exists between the two. In both cases the threshold of the primary bifurcation lies between $G = 150$ and 160. The axisymmetry breaking arising in the wake generates a steady lift, making the unconfined sphere drift, in principle infinitely, in a vertical plane. A sphere confined in a circular tube is immediately exposed to a repulsive wake–wall interaction. Contrary to expectation, there is no stable state corresponding to static equilibrium of the lift and repulsion from the wall. Instead, at near-critical Galileo numbers, the sphere tends to oscillate in a (probably arbitrary) plane before switching to a helical trajectory. The latter presents the counterpart of the steady oblique trajectory of an unconfined sphere.

The unconfined sphere undergoes a secondary instability at about $G = 190$ for $\rho_s/\rho = 2$, the case mostly investigated in the present paper. This instability leads to an unsteady periodic regime called the oblique oscillating state in Jenny *et al.* (2004). The sphere confined to a tube undergoes an instability, triggering an unsteady wake earlier, between $G = 170$ and 180. This might be explained by the excitation of the helical state by higher harmonics, making the distance between the sphere and the wall oscillate. Incidentally, the vortex shedding frequency is close to the fifth harmonic of the primary regime. The vortex shedding frequency does not eventually either lock in within a new periodic state or combine in a quasiperiodic state. Instead, the vortex shedding disappears at moments when the sphere approaches the wall and the growth rate of the vortex shedding brings about an additional time scale leading to intermittency.

Due to computing costs and stability limits of the code at low density ratios, the effect of the density ratio has been only partly investigated. It seems, nevertheless, that there may be a link to the striking behaviour of the oblique steady regime of an unconfined sphere, for which a jump in vortex shedding frequency was exhibited between $\rho_s/\rho = 2$ and 3. In the present case this jump is likely to lie a little higher, as shown by comparing the simulations at $\rho_s/\rho = 3$ and 5.

The results obtained may be of use for understanding the sedimentation in many particle systems confined in circular pipes, both in a quiescent fluid and in a developed pipe flow.

Acknowledgements

The authors would like to acknowledge the Direction Informatique (Pôle HPC) of the University of Strasbourg and CINES/GENCI France (platform JADE) for supporting this work by providing scientific support and access to computing resources.

Supplementary material

A supplementary movie is available at http://dx.doi.org/10.1017/jfm.2012.362.

REFERENCES

BAGCHI, P. & BALACHANDAR, S. 2002 Effect of free rotation on the motion of a solid sphere in linear shear flow at moderate *Re*. *Phys. Fluids* **14**, 2719.

BORAZJANI, I., GE, L. & SOTIROPOULOS, F. 2008 Curvilinear immersed boundary method for simulating fluid structure interaction with complex 3D rigid bodies. *J. Comput. Phys.* **227**, 7587–7620.

CHORIN, A. J. 1968 Numerical solution of the Navier–Stokes equations. *J. Math. Comput.* **22**, 745.

DANAILA, I., DUŠEK, J. & ANSELMET, F. 1998 Nonlinear dynamics at a Hopf bifurcation with axisymmetry breaking in a jet. *Phys. Rev.* E **57**, 3695–3698.

DELOZE, T., HOARAU, Y. & DUŠEK, J. 2010 Chimera method applied to the simulation of a freely falling cylinder in a channel. *Eur. J. Comput. Mech.* **19**, 575–590.

FENG, J., HU, H. H. & JOSEPH, D. D. 1994 Direct simulation of initial value problems for the motion of solid bodies in a Newtonian fluid. Part 1. Sedimentation. *J. Fluid Mech.* **261**, 95–134.

GHIDERSA, B. & DUŠEK, J. 2000 Breaking of axisymmetry and onset of unsteadiness in the wake of a sphere. *J. Fluid Mech.* **423**, 33–69.

GLOWINSKI, R., PAN, T. W., HESLA, T. I., JOSEPH, D. D. & PERIAUX, J. 2001 A fictitious domain approach to the direct numerical simulation of incompressible viscous flow past moving rigid bodies: application to particulate flow. *J. Comput. Phys.* **169** (2), 363–426.

HU, H. H., PATANKAR, N. A. & ZHU, M. Y. 2001 Direct numerical simulations of fluid–solid systems using the arbitrary Lagrangian–Eulerian technique. *J. Comput. Phys.* **169** (2), 427–462.

JENNY, M., BOUCHET, G. & DUŠEK, J. 2003 Nonvertical ascension or fall of a free sphere in a Newtonian fluid. *Phys. Fluids* **15**, L9.

JENNY, M. & DUŠEK, J. 2004 Efficient numerical method for the direct numerical simulation of the flow past a single light moving spherical body in transitional regimes. *J. Comput. Phys.* **194**, 215–232.

JENNY, M., DUŠEK, J. & BOUCHET, G. 2004 Instabilities and transition of a sphere falling or ascending freely in a Newtonian fluid. *J. Fluid Mech.* **508**, 201–239.

JEONG, J. & HUSSAIN, F. 1995 On the identification of a vortex. *J. Fluid Mech.* **285**, 69–94.

JOHNSON, T. A. & PATEL, V. C. 1999 Flow past a sphere up to a Reynolds number of 300. *J. Fluid Mech.* **378**, 19–70.

KARNIS, A., GOLDSMITH, H. L. & MASON, S. G. 1966 The flow of suspensions through tubes. Part 5. Inertial effects. *Can. J. Chem. Engng* **44** (4), 181–193.

KOTOUČ, M., BOUCHET, G. & DUŠEK, J. 2009 Transition to turbulence in the wake of a fixed sphere in mixed convection. *J. Fluid Mech.* **625**, 205–248.

KUROSE, R. & KOMORI, S. 1999 Drag and lift forces on a rotating sphere in a linear shear flow. *J. Fluid Mech.* **384**, 183–206.

MATAS, J. P., MORRIS, J. F. & GUAZZELLI, E. 2004 Inertial migration of rigid spherical particles in Poiseuille flow. *J. Fluid Mech.* **515**, 171–195.

NAMKOONG, K., YOO, J. Y. & CHOI, H. G. 2008 Numerical analysis of two-dimensional motion of a freely falling circular cylinder in an infinite fluid. *J. Fluid Mech.* **604**, 33–53.

ORMIÈRES, D. & PROVANSAL, M. 1999 Transition to turbulence in the wake of a sphere. *Phys. Rev. Lett.* **83**, 80–83.

SAFFMAN, P. G. 1965 The lift on a small sphere in a slow shear flow. *J. Fluid Mech.* **22**, 385–400.

SEGRÉ, G. 1961 Radial particle displacements in Poiseuille flow of suspensions. *Nature* **189**, 209–210.

SEGRÉ, G. & SILBERBERG, A. 1962 Behaviour of macroscopic rigid spheres in Poiseuille flow. Part 1. Determination of local concentration by statistical analysis of particle passages through crossed light beams. *J. fluid Mech.* **14** (01), 115–135.

TAKEMURA, F. & MAGNAUDET, J. 2003 The transverse force on clean and contaminated bubbles rising near a vertical wall at moderate Reynolds number. *J. Fluid Mech.* **495**, 235–253.

TAKEMURA, F., TAKAGI, S., MAGNAUDET, J. & MATSUMOTO, Y. 2002 Drag and lift forces on a bubble rising near a vertical wall in a viscous liquid. *J. Fluid Mech.* **461**, 277–300.

TOMBOULIDES, A. G. & ORSZAG, S. A. 2000 Numerical investigation of transitional and weak turbulent flow past a sphere. *J. Fluid Mech.* **416**, 45–73.

UHLMANN, M. 2005 An immersed boundary method with direct forcing for the simulation of particulate flows. *J. Comput. Phys.* **209**, 448–476.

VELDHUIS, C. H. J. & BIESHEUVEL, A. 2007 An experimental study of the regimes of motion of spheres falling or ascending freely in a Newtonian fluid. *Intl J. Multiphase Flow* **33** (10), 1074–1087.

VOS, J., RIZZI, A., DARRACQ, D. & HIRSCHEL, E. 2002 Navier–Stokes solvers in European aircraft design. *Prog. Aerosp. Sci.* **38**, 601–697.

YANG, B. H., WANG, J., JOSEPH, D. D., HU, H. H., PAN, T. W. & GLOWINSKI, R. 2005 Migration of a sphere in tube flow. *J. Fluid Mech.* **540**, 109–131.

YU, Z., PHAN-THIEN, N., FAN, Y. & TANNER, R. I. 2002 Viscoelastic mobility problem of a system of particles. *J. Non-Newtonian Fluid Mech.* **104** (2–3), 87–124.

YU, Z., PHAN-THIEN, N. & TANNER, R. I. 2004 Dynamic simulation of sphere motion in a vertical tube. *J. Fluid Mech.* **518**, 61–93.

ZENG, L., BALACHANDAR, S. & FISCHER, P. 2005 Wall-induced forces on a rigid sphere at finite Reynolds number. *J. Fluid Mech.* **536**, 1–25.